

Document downloaded from:

<http://hdl.handle.net/10251/111689>

This paper must be cited as:

Balaguer-Puig, M.; Marqués-Mateu, Á.; Lerma García, JL.; Ibañez Asensio, S. (2017). Estimation of small-scale soil erosion in laboratory experiments with Structure from Motion photogrammetry. *Geomorphology*. 295:285-296. doi:10.1016/j.geomorph.2017.04.035



The final publication is available at

<https://doi.org/10.1016/j.geomorph.2017.04.035>

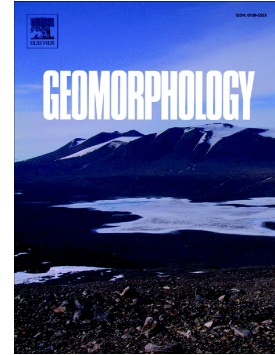
Copyright Elsevier

Additional Information

Accepted Manuscript

Estimation of small-scale soil erosion in laboratory experiments with Structure from Motion photogrammetry

Matilde Balaguer-Puig, Ángel Marqués-Mateu, José Luis Lerma, Sara Ibáñez-Asensio



PII: S0169-555X(16)31173-4
DOI: doi: [10.1016/j.geomorph.2017.04.035](https://doi.org/10.1016/j.geomorph.2017.04.035)
Reference: GEOMOR 6016
To appear in: *Geomorphology*
Received date: 12 December 2016
Revised date: 22 April 2017
Accepted date: 24 April 2017

Please cite this article as: Matilde Balaguer-Puig, Ángel Marqués-Mateu, José Luis Lerma, Sara Ibáñez-Asensio , Estimation of small-scale soil erosion in laboratory experiments with Structure from Motion photogrammetry, *Geomorphology* (2017), doi: [10.1016/j.geomorph.2017.04.035](https://doi.org/10.1016/j.geomorph.2017.04.035)

This is a PDF file of an unedited manuscript that has been accepted for publication. As a service to our customers we are providing this early version of the manuscript. The manuscript will undergo copyediting, typesetting, and review of the resulting proof before it is published in its final form. Please note that during the production process errors may be discovered which could affect the content, and all legal disclaimers that apply to the journal pertain.

Estimation of small-scale soil erosion in laboratory experiments with Structure from Motion photogrammetry

Matilde Balaguer-Puig¹, Ángel Marqués-Mateu¹, José Luis Lerma¹, Sara Ibáñez-Asensio²

¹ Department of Cartographic Engineering, Geodesy and Photogrammetry, Universitat Politècnica de València, Camino de Vera, s/n 46022 Valencia (Spain)

² Department of Plant Production, Universitat Politècnica de València, Camino de Vera, s/n 46022 Valencia

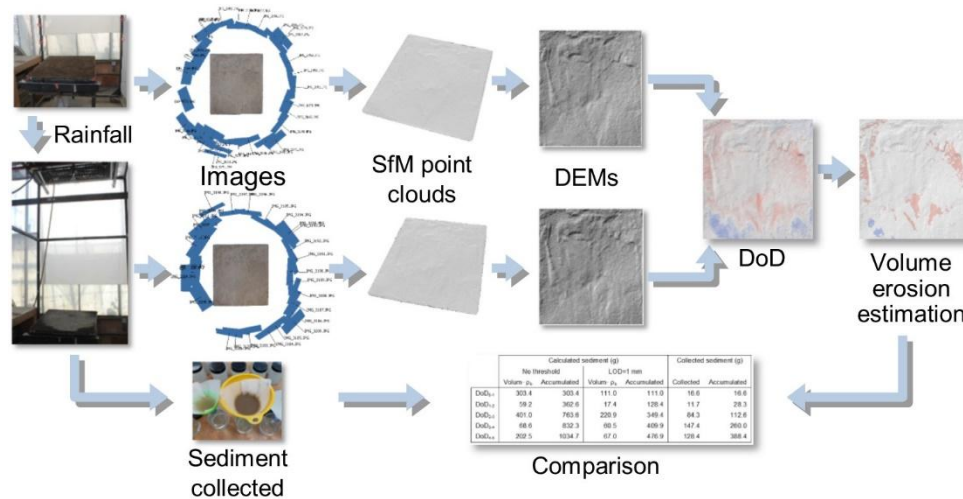
Corresponding author:

Matilde Balaguer Puig (balaguer@upv.es) Department of Cartographic Engineering, Geodesy and Photogrammetry, Camino de Vera, s/n 46022 Valencia

Highlights

- Convergent SfM provides reliable DEMs for microscale geomorphic change detection.
- Reliable results require rigorous DEMs georeferencing in a local reference system.
- Comparison with dragged sediment in runoff shows good agreement.
- Basic LOD_{min} thresholding shows right performance to detect tiny changes.

Graphical Abstract



Abstract

The quantitative estimation of changes in terrain surfaces caused by water erosion can be carried out from precise descriptions of surfaces given by means of digital elevation models (DEMs). Some stages of water erosion research efforts are conducted in the laboratory using rainfall simulators and soil boxes with areas less than 1 m². Under these conditions, erosive processes can lead to very small surface variations and high precision DEMs are needed to account for differences measured in millimetres. In this paper, we used a photogrammetric Structure from

Motion (SfM) technique to build DEMs of a 0.5 m² soil box to monitor several simulated rainfall episodes in the laboratory. The technique of DEM of difference (DoD) was then applied using GIS tools to compute estimates of volumetric changes between each pair of rainfall episodes. The aim was to classify the soil surface into three classes: erosion areas, deposition areas, and unchanged or neutral areas, and quantify the volume of soil that was eroded and deposited. We used a thresholding criterion of changes based on the estimated error of the difference of DEMs, which in turn was obtained from the root mean square error of the individual DEMs. Experimental tests showed that the choice of different threshold values in the DoD can lead to volume differences as large as 60% when compared to the direct volumetric difference. It turns out that the choice of that threshold was a key point in this method. In parallel to photogrammetric work, we collected sediments from each rain episode and obtained a series of corresponding measured sediment yields. The comparison between computed and measured sediment yields was significantly correlated, especially when considering the accumulated value of the five simulations. The computed sediment yield was 13% greater than the measured sediment yield. The procedure presented in this paper proved to be suitable for the determination of sediment yields in rainfall-driven soil erosion experiments conducted in the laboratory.

Keywords

Erosion, Photogrammetry, Structure from Motion (SfM), Digital Elevation Models (DEM), DEM of Difference (DoD), Geographical Information Systems (GIS)

1. Introduction

The rigorous modelling and quantification of soil water erosion processes requires detailed information about the topography of the land surface with appropriate resolution and accuracy. In the field of soil erosion research, one approach has been to conduct experiments using rainfall simulators to measure rainfall-driven soil erosion from soil plots of small dimensions. Determining soil topography and estimating its variation in each erosive stage is currently conducted by means of digital elevation model (DEM) analyses. DEMs have been routinely obtained by means of photogrammetric and laser scanning surveys. In addition to the classical stereoscopic photogrammetry approach, a recent variant known as Structure from Motion (SfM), based on

automatic image registration methods and image matching algorithms, is gaining recognition in soil science, geomorphology and other related disciplines (Westoby et al., 2012; Fonstad et al., 2013; Micheletti et al., 2015; Carrivick et al., 2016; Eltner et al., 2016; Smith et al., 2016). The study presented in this paper relies upon photogrammetric SfM techniques to generate the DEMs, which are the basis for erosion computations.

The precise description of the soil surface topography and how it changes during the erosion process is a necessity for soil erosion studies at millimetre scales (Rieke-Zapp and Nearing, 2005). At the microscale, soil surface information can be retrieved with a number of methods that are grouped into contact and non-contact techniques (Jester and Klik, 2005). Classical contact techniques require specific instruments such as the roller chain (Saleh, 1993; Merrill et al., 2001) or pin meter (Kuipers, 1957; Huggins, 1981; Podmore and Vidal Vázquez, 2003; Moreno et al., 2008). Non-contact techniques depend on the use of some sort of electronic device such as the Instantaneous-Profile Laser Scanner (Bertuzzi et al., 1990; Darboux and Huang, 2003; Li and Chen, 2012), terrestrial laser scanners (TLS) (Huang and Bradford, 1992; Haubrock et al., 2009; Afana et al., 2010) and photogrammetry (Butler et al., 1998; Chandler, 1999; Rieke-Zapp et al., 2001; Lascelles et al., 2002; Rieke-Zapp and Nearing, 2005).

Some of the research on small scale rainfall-driven soil erosion is carried out using direct measurements on experimental plots, either in the field or in the laboratory. Plot measurements provide actual data that can be compared to the outcomes from predictive models. Erosion experiments are conducted in specifically designed runoff plots with characteristics that may vary depending on the scale and type of study. Through the use of different types of collectors coupled to the experimental plot, runoff and sediment for subsequent processing can be collected. Boix-Fayos et al. (2006) studied the advantages and limitations of using field plots to measure soil erosion and possible sources of variation in the results. Field measurements under natural rain conditions have the advantage of working at the correct scale with actual soil characteristics and temporal changes in environmental variables. However, disadvantages include the long periods of time necessary to analyse the evolution, the inability to control and isolate variables and parameters, and the difficulty in comparing results. Because of these drawbacks, the use of rainfall simulators is common practice in both field and laboratory experiments.

Rainfall simulators are devices developed to mimic the characteristics of rainfall as closely as possible, reproducing both the distribution of droplet sizes as well as its kinetic energy of impact (Cerdà, 1999). Simulators are routinely used to study rainfall-runoff relationships, infiltration rates, and estimate soil loss. One of the main advantages is that by not relying on natural rain, it is possible to maintain stricter schedules and perform many more experiments in a short time period. Laboratory experiments use rainfall simulators placed over small plots which are basically trays or boxes filled with disturbed soil samples and prepared under specific conditions. Those soil boxes are designed to reproduce free draining conditions and integrate specific devices to vary soil slope and collect data on infiltration, runoff and sediment yield. Laboratory conditions provide an improved control of the variables under study and offer the possibility of using advanced equipment and replicate measurements (Stroosnijder, 2005).

The detection and quantification of geomorphological changes over time can be performed through comparison of topographic surfaces or DEMs at different time intervals. This approach is known as geomorphic change detection (GCD), and is based on the analysis of DEMs of Differences (DoD) (Wheaton et al., 2010), whereby the estimates of volumetric changes are obtained from differences of elevations between sequential DEMs of the same zone. Those surface changes can be quantified in terms of erosion and sediment yield. This approach has been widely used in geomorphology and related disciplines (see Williams, 2012, for detailed compilation of studies in various fields), and in particular in soil erosion studies, at scales that range from medium (e.g., Lane et al., 2003; Martínez-Casasnovas, 2003; Milan et al., 2011; James et al., 2012) to small (e.g., Marzoff and Poesen, 2009) to microscale (e.g., Gessesse et al., 2010).

Photogrammetry is a widely accepted technique used to acquire spatial datasets intended to build DEMs. Previous work on DEM generation in small experimental plots by photogrammetry has been typically performed using images obtained with consumer-grade digital cameras and classical stereoscopic photogrammetry with vertical images (Lascelles et al., 2002; Rieke-Zapp and Nearing, 2005; Gessesse et al., 2010) or convergent image pairs (Heng et al., 2010; Moritani et al., 2011).

The current trend in photogrammetry follows a three-dimensional (3D) modelling approach that combines two processes, SfM and MultiView Stereo Matching (MVS), which are the results of advances in the fields of computer vision and image processing. This approach, usually named SfM-MVS photogrammetry, allows users to solve simultaneously and automatically the camera pose and the geometry of the scene, without ground control points (GCP), from automatically extracted features given a set of overlapping images (Westoby et al., 2012). SfM is based on feature detection algorithms to identify features or points of interest that are invariant to scale changes and rotations in the initial images. Next, those points extracted from each individual image are properly linked by a matching algorithm, determining the sets of homologous points (i.e., image points in several pictures of the same object point). The procedure determines existing features between each pair of images, and calculates the corresponding orientation matrix. Based on these results, the best pair of images is chosen as the initial dataset for the 3D scene reconstruction with MVS. Finally, an iterative bundle adjustment (which may add more images in order to optimise the parameters computations) gives a collection of 3D points, the point cloud, in an arbitrary coordinate system (Yang et al., 2013). The user can then apply a 3D transformation to the point cloud so that the cloud is scaled and referenced in a specific local reference system. This transformation is only possible if there is a minimum of three ground control points (GCPs).

Carrivick et al. (2016) published a detailed analysis of the SfM technology, advantages and disadvantages, and its application to geosciences, and concluded that it is a suitable alternative for terrain modelling, independently of the spatial scale. The accuracy of SfM point clouds has been analysed using 3D data obtained with other techniques (e.g., TLS) as benchmark (e.g., James and Robson, 2012; Kaiser et al., 2014; Smith and Vericat, 2015), showing good concordance. Fonstad et al. (2013) presented a detailed description of the method and applied it to obtain a 3D model of a river area from low-altitude aerial images with results comparable to Lidar surveys. Eltner et al. (2016) reviewed the current status of implementation of the SfM methodology in geomorphometry (they gathered a collection of terms, software tools and publications since 2012) and conducted a detailed evaluation of errors in SfM photogrammetry. Other studies applied the SfM methodology at different scales (James and Robson, 2012; Gómez-Gutiérrez et al., 2014) to calculate terrain roughness parameters in small plots (Bretar et al., 2013; Snapir et al., 2014) or in the laboratory

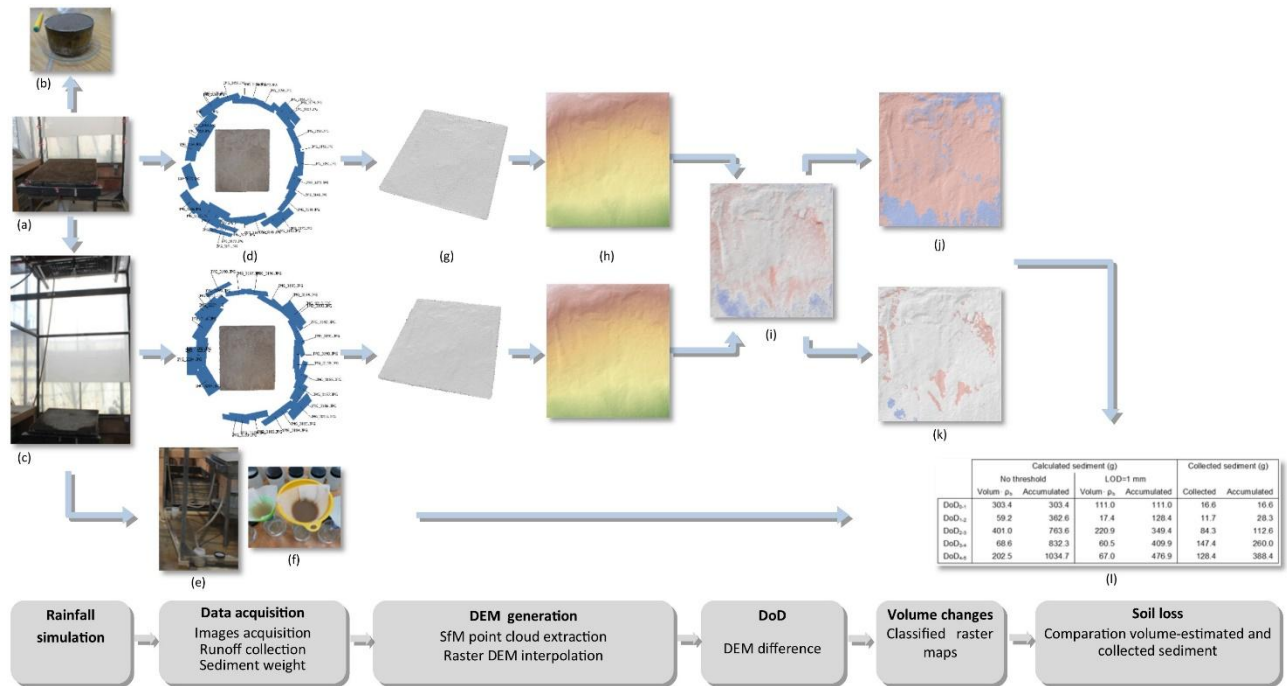
(Nouwakpo et al., 2014; Morgan et al., 2017). Those research efforts demonstrate the utility of SfM photogrammetric methods in geomorphological studies at small and micro scales in natural terrain. Under such conditions, SfM provides accurate DEMs and the aforementioned advantages of ease of use, flexibility and low cost. However, its performance in applications requiring fine resolution and high precision DEMs (mm), for instance precise water erosion studies in the laboratory, is still in experimental stages. Kasprak et al. (2015) used SfM to generate DEMs with a relative vertical accuracy of 2 mm in sediment transport studies with laboratory flumes. Nouwakpo et al. (2014) conducted a study on a soil box of 9.75 x 3.66 m with a rainfall simulator and SfM photogrammetry, but used non-convergent image configuration with vertical pictures taken from a sliding platform located onto the box. Hänsel et al. (2016) used rainfall simulation and SfM with convergent images in field plots located in agricultural fields, and compared soil loss estimated by volumetric changes with a estimation of soil loss by sampling of suspended sediments. In contrast, in laboratory experiments actual sediments can be collected, providing a reliable validation of volumetric changes.

In this paper we present a laboratory procedure to determine the sediment balance using a geomorphological change detection approach, with DoDs from DEMs generated with photogrammetric SfM in a convergent multi-image configuration. The goal is to achieve fine resolution, high precision DEMs, able to provide reliable DoDs and sediment budgets in surfaces with small changes caused by low intensity rain. In this regard, establishing a coordinate reference system (CRS) for rigorous georeferencing of DEMs and defining an appropriate threshold to differentiate changes from errors is essential. The results will be validated by direct comparison of the morphological budget approach estimates with the actual sediment yield collected in the experiments, which acts as “ground truth”.

2. Material and methods

Fig. 1 shows the sequence of stages in the procedure as consisting of (1) the rainfall simulation experiment, (2) data acquisition (images, runoff and infiltration collection, bulk density and weight of sediment yield computation), (3) DEM generation (SfM point cloud extraction and raster DEM interpolation), (4) DoD (differences of image-generated DEMs), (5) volumetric change calculation

and classification in terms of erosion, and (6) comparison of soil loss derived from the DEM-based



estimation with actual sediment measurements.

Fig. 1. Working scheme: Rainfall simulation experiment: (a) Preparation of box with soil sample, positioning and measurement of reference signals; (b) Undisturbed soil sample for bulk density calculation; (c) Rainfall simulation; Data acquisition: (d) Image acquisition before and after rain; (e) Runoff collection during rain simulation; (f) Filtering and weighting sediments; DEM generation: (g) SfM point cloud extraction; (h) Raster DEM generation; DoD: (i) Difference of successive DEMs; Volumetric changes: Estimation of volumetric change from DEM differences and classification in erosion (red), deposition (blue) and unchanged (grey) classes: (j) without threshold, and (k) with $LOD_{min} = 1$ mm; Soil loss: (l) Calculation of soil loss from volume (through soil bulk density) and comparison with soil collected in runoff.

2.1. Rainfall simulation experiment

The setup of the experiment to measure surface runoff and sediment yield in the laboratory consisted of a small box of soil (68 x 75 cm) with a uniform slope of 10%, without vegetation cover, subjected to simulated rain with a constant intensity in successive episodes of varying duration.

The indoor rainfall simulator (Fig. 2) was based on a classical design (Cerdà et al., 1997), formed by a metallic structure of dimensions 3.10 x 1.60 x 2.00 m (height x width x depth) supporting the droplet generating mechanism horizontally at 2 m above the soil box (Fig. 2a). The generator mechanism was a rain spray nozzle installed in a PVC hose, fixed to a metal bar attached to the top of the simulator structure (Fig. 2b). A regulating pressure gauge controlled the nozzle hydraulic

circuit to ensure constant pressure throughout the simulation. This regulator equipment was located next to the simulator (Fig. 2c). The working pressure established for the entire simulation was 2.3 bar and the rainfall intensity applied was 30 mm/h. A spray nozzle was selected instead of a dropper

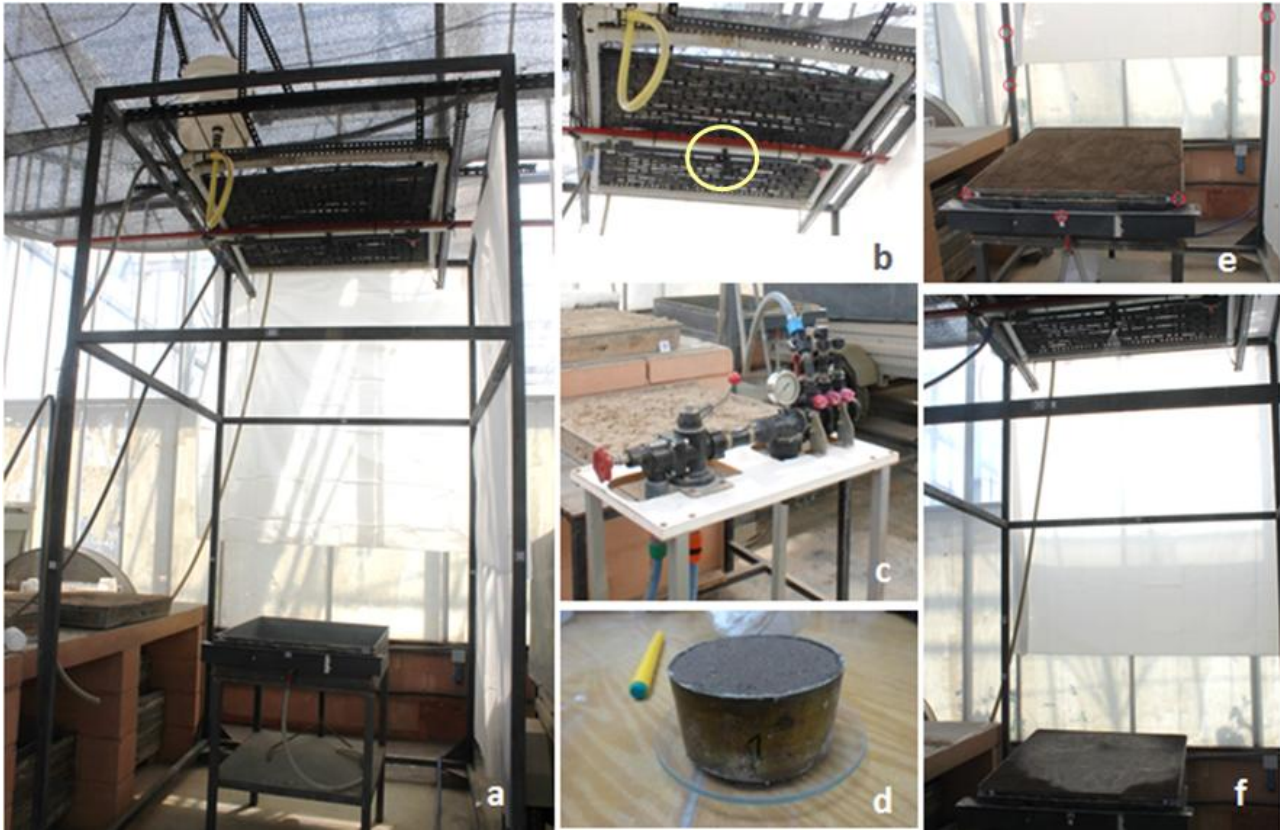


Fig. 2. Rainfall simulation experiment: (a) Rainfall simulator and simulation table; (b) Rain spray nozzle; (c) Regulator pressure equipment; (d) Undisturbed soil sample (cylinder dimensions: diameter 5.5 cm, height 3 cm); (e) Prepared soil box with GCPs; (f) Simulation of rain on the soil box.

to reduce the effect of splash erosion by reducing the size of the drop (Hancock and Willgoose, 2001). As a result, the amount of sediment that could jump out of the box, and thus avoid collection in our experiment, was not significant for the rain intensity and droplet size used in the simulation.

Under this structure, a simulation table installed at a height of 1 m above the ground, supported a box (dimensions 68 x 75 cm and surface 0.5 m²) containing the soil sample. The table had a system to gather surface runoff so that both water and eroded sediment were collected by a gutter located on the front that poured into a container through a flexible PVC hose (Fig. 2a). On the back of the table, a screw mechanism enabled the box to be lifted, which was adjusted so that the soil surface had a slope of 10%. The soil sample was prepared by placing a layer of small pieces of expanded polystyrene (3 x 2 cm) in the bottom of the box to allow the drainage of infiltrated water.

Then, a textile mesh was laid over the polystyrene layer to prevent loss of sediment. A 10 cm layer of natural sandy soil, without coarse fragments, was prepared by moistening it repeatedly to get the homogeneous bulk density and compaction similar to the natural soil throughout the box. Once ready, and before starting the simulations, undisturbed soil samples were taken with the core method for subsequent bulk density calculations (Fig. 2d). Once the soil box was placed on the simulation table, and conveniently located below the spray nozzle, a series of signalised ground control points (GCP) were distributed on the table and simulator structures (Fig. 2e). A total station (TST) was then used to carry out the necessary measurements to give coordinates to these point signals in a local Cartesian reference system with the Z axis coincident with the local vertical direction. This reference system was used for subsequent positioning and DEM comparison purposes. Fig. 2f shows the simulator running for one of the rain simulations.

2.2. Data acquisition

Before starting the first rainfall simulation, a number of images of the soil surface were taken. This dataset as well as the models generated from the pictures were numbered as 0 (initial). Five consecutive rain simulations of different durations were executed as follows: an initial simulation of 15 min, followed by one of 30 min, and then three more simulations of 60 min each. After every single episode, we measured runoff and infiltration and took a new set of pictures. These datasets were numbered from 1 to 5.

2.2.1. Image acquisition

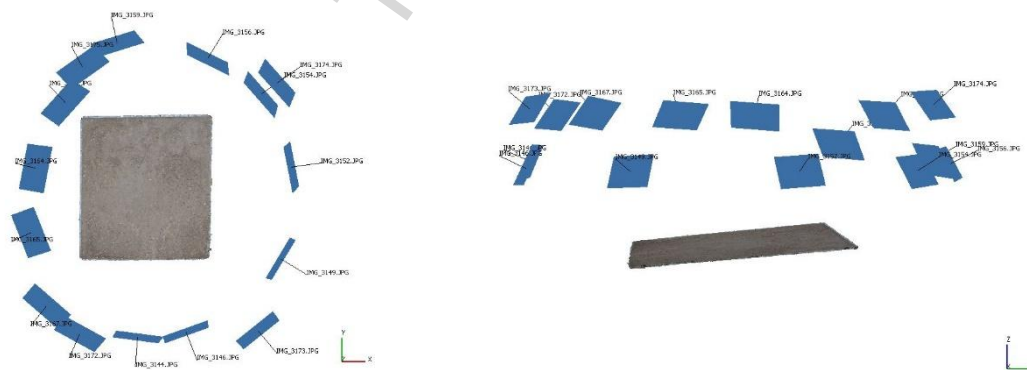
A digital camera Canon EOS 1100D SLR with variable zoom lens Canon EF-S 18-55 mm was used. The scheme to collect images was an adaptation of the 3 x 3 CIPA standards for dense image matching methods (Wenzel et al., 2013). Convergent oblique images were taken around the object with high redundancy. This network image geometry provides the highest accuracy in photogrammetric point measurement (Luhmann et al., 2013) and reduces systematic errors in 3D models which are caused by inaccurately estimated lens distortion parameters (Wackrow and Chandler, 2011; James and Robson, 2014). The theoretical error obtained in determining the coordinates of an object point viewed in k images using the principles of close range photogrammetry with multiple converging images is given by the expression (Fraser, 1996; Barazzetti et al., 2010; James and Robson, 2012; Luhmann et al., 2013):

$$\sigma_c = \frac{q \cdot D}{f \cdot \sqrt{k}} \cdot \sigma_i \quad (1)$$

where q is an empiric design factor related to the geometry of the photogrammetric network ranging between 0.4 and 2, D is the camera-object distance, f is the focal length, and σ_i is the measurement accuracy in the image.

Eq. (1) can be used to determine the maximum camera-object distance according to the desired object precision. In the case of a survey with converging images with complete coverage of the object, one can consider standard values $q = 1$ and $k = 3$ (James and Robson, 2012; Eltner et al., 2016). Assuming that the measurement accuracy in the image is $\sigma_i = 10 \mu\text{m}$ (1 pixel), focal length $f = 18 \text{ mm}$, and a desired precision $\sigma_c = 0.5 \text{ mm}$, the maximum object distance obtained from Eq. (1) is $D = 1.56 \text{ m}$.

Images were taken at an average distance of 0.5 m from the simulation table, thus achieving camera-object distances less than 1.5 m for all object points. Shot locations were distributed following a ring-shaped path around the object following a convergent set up to strengthen the network, with a step size between consecutive images of 0.3 m, and at different heights to reinforce the adjustment geometry (Fig. 3). The principal distance selected was 18 mm with an f-number of $f/22$ for the whole survey. The ground sampling distance (GSD) was 0.28 mm at a



distance of 0.5 m.

Fig. 3. Distribution of images around the simulation table: a) top view; b) right view.

2.2.2. Collection of runoff and infiltration

After every rainfall episode, runoff and infiltration data produced in the soil box were collected using plastic containers. The average time to fill the containers was 4 min (longer at the beginning

of the experiment and shorter as the soil became saturated). A total of 45 runoff and 10 infiltration containers were collected.

The weight of the sediments transported by runoff and infiltration was obtained by standard laboratory methods of weighing samples that had been filtered and oven-dried at 105°C to a constant weight. The bulk density was determined before and after the rain simulations, using the core method (Chan, 2006). We obtained an average value of 1.43 g/cm³.

2.3. DEM generation

Six point clouds were created following the standard SfM-MVS workflow (e.g., Carrivick et al., 2016) using the software Agisoft PhotoScan. We set up the camera model using the calibration file (previously obtained with Agisoft calibration tool) and considering these parameters as initial or pre-calibrated values. Then we set the local CRS by measuring the signalised GCPs on all the images. The probability of having distorted point clouds caused by inaccurate modelling of the radial lens distortion is significantly reduced whenever convergent oblique images are taken and GCPs are included in the adjustment (James and Robson, 2014). The orientation of the images was carried out automatically using feature matching and bundle adjustment. Finally, dense point clouds were created with MVS algorithms, using image masks to restrict the calculation of points specifically to the area of interest.

A raster DEM with a cell size of 1 mm was created from each one of the six dense point clouds, using the inverse distance weighting (IDW) interpolation method in the ArcGIS environment. We used geostatistical tools to determine the height interpolation error by means of the split-sample validation technique (Smith et al., 2005; Erdogan, 2009). The check points set were created with a random selection of 5% of the original point cloud.

The 3D geometric transformation used to convert point clouds to the desired reference system is considered a source of error in the DEMs, and the root mean square error (RMSE) of the GCPs used in the bundle adjustment is an estimate of this transformation error (Heng et al., 2010; James and Robson, 2012). Therefore, according to the “prediction by production” approach of Li et al. (2005), the total DEM error considered in this paper follows the quadratic composition of two error

components: the error of the geometric transformation of point clouds to the local CRS, E_T , and the interpolation error E_I .

$$E_{DEM} = \sqrt{(E_T^2 + E_I^2)} \quad (2)$$

The assessment of accuracy in the DEMs is usually carried out by checking a number of cell elevations against a set of high precision, uniformly distributed check points (Li et al., 2005). However, some practical problems arise in geomorphological studies where the surface represented by the DEMs undergoes morphological changes. That is the case in rainfall simulation studies in which it is not possible to place control points that remain fixed on the soil surface without experiencing changes in their position during rain or otherwise affecting the phenomenon under study. However, the goal was to compare various surfaces, created with the same method and quality, with each other. The absolute accuracy of measured elevations is not relevant (Reuter et al., 2009). The interest focused specifically on the relative accuracy of the surface determination.

2.4. DoDs

DEMs were subtracted on a cell-by-cell basis giving DoDs or maps of differences. The DoDs were then reclassified so that negative values denoted erosion cells and positive values denoted deposition cells. Using the bulk density value, weights corresponding to erosion, deposition, and net soil loss were determined.

The computation of a DoD as the difference of two DEMs can propagate the errors of the initial DEMs, so an error analysis is necessary to produce reliable results. This is especially true when the magnitude of geomorphic change is similar to the magnitude of uncertainties of the DEMs. In the field of geomorphological analysis, several change detection techniques that provide thresholded DoDs based on an error assessment have been used in previous research. Some examples include (1) applying a minimum level of detection, (2) obtaining a probabilistic thresholding, (3) considering the spatial variability of uncertainty from multiple parameters, and (4) assessing the spatial coherence of erosion and deposition (Williams, 2012). As stated elsewhere, we did not use check/control points on the surface, which is a requirement to apply probabilistic thresholding. Furthermore, we did not determine the spatial coherence of erosion and deposition, and the spatial variation of surface parameters such as slope or roughness were fairly uniform on

the soil plot. These are attributes that have been used in previous research to apply spatially distributed thresholding methods. Therefore, based on the characteristics of this study, we chose the minimum level of detection (LOD_{min}) approach.

A common estimate of the error in the difference of two DEMs is the quadratic composition of errors in each of the original DEMs being compared (Brasington et al., 2003; Lane et al., 2003; Wheaton et al., 2010; Williams, 2012; Gómez-Gutiérrez et al., 2014):

$$E_{DoD_{1-2}} = \sqrt{(E_{DEM_1}^2 + E_{DEM_2}^2)} \quad (3)$$

Assuming known values for E_{DEM_1} and E_{DEM_2} , Eq. (3) can be applied globally, or locally if the spatial variation of the error of each of the DEMs is known (Lane et al., 2003). This paper assumes that the error in the DEM follows a global uniform spatial distribution. In order to apply the minimum threshold level of detection LOD_{min} , the value E_{DoD} obtained from Eq. (3) was employed as a constant threshold to the calculated DEM difference (Williams, 2012):

$$LOD_{min} = E_{DoD} \quad (4)$$

Elevation differences greater than this threshold are considered reliable, while those that are below are considered noise. In other words, it is not possible to reliably detect elevation changes within the range $[-LOD_{min}, +LOD_{min}]$ (Wheaton et al., 2010). The LOD_{min} approach is simple and easy to implement, but it discards more information as LOD_{min} increases. It is for this reason that the numerical threshold value must be chosen very carefully based on a rigorous design of the experimental setup.

We designed a custom tool in the ArcMap working environment to automate the creation of DoDs and the reclassification of the results from LOD_{min} and bulk density values. The output for each DoD consists of a raster map with elevation differences, another raster map classified as erosion, deposition or unchanged areas, and a text file with the numerical results (minimum and maximum values of elevation differences, and number of cells, area and volume of each erosion class).

3. Results and discussion

3.1. Point clouds

The six point clouds, corresponding to the initial situation (Cloud 0) and the time after each of the

five episodes of rain (Clouds 1 to 5) were obtained using the photogrammetric SfM workflow. The number and density of points obtained are fairly homogeneous (Table 1).

Table1 Characteristics of point clouds.

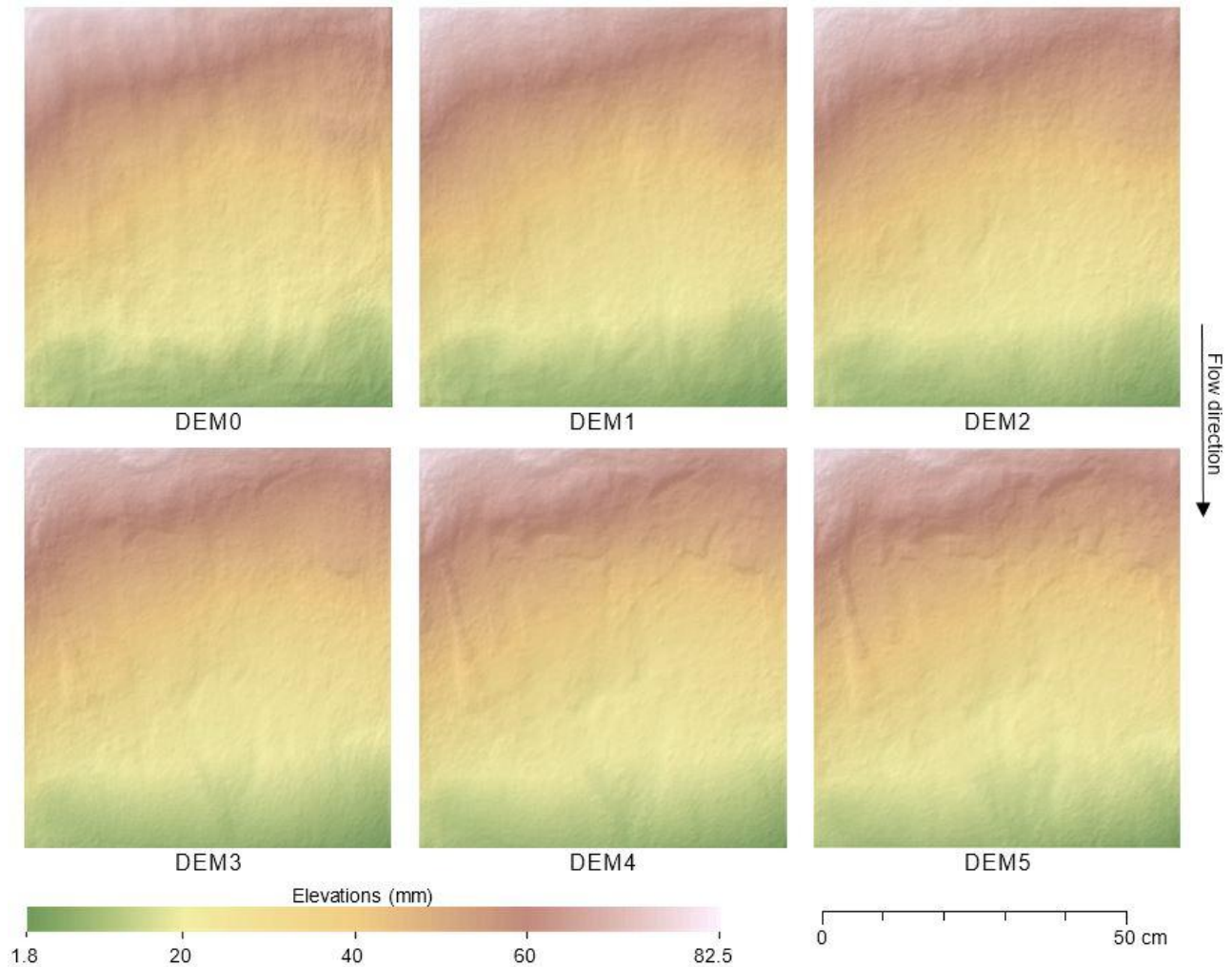
Cloud	No. points	Points/cm ²	Spacing (mm)
Cloud 0	620 136	1 240	1.3
Cloud 1	746 967	1 494	1.2
Cloud 2	747 344	1 495	1.2
Cloud 3	779 508	1 559	1.1
Cloud 4	741 073	1 482	1.2
Cloud 5	750 096	1 500	1.2

Although the photogrammetric SfM methodology allows us to create point clouds with arbitrary position and orientation, in our study we needed to ensure that the georeferencing and scale were exactly the same in all the clouds to make further comparisons between them. The identification and measurement of GCPs that define the CRS can be done on the initial images or on the point clouds, although it is more reliable on the images (James and Robson, 2012). In our study, we measured GCPs on the images. The orientation of the images and the coordinates of the point clouds were then obtained directly in the proper CRS. The georeferencing error of the point clouds was estimated with the RMSE of the spatial transformation of the GCPs which varied from 0.516-0.803 mm, with a mean value of 0.654 mm. The relative error, i.e., the ratio of measured error to camera-object distance (Eltner et al., 2016) assuming the largest one of 1.5 m, is 1:2294. Theoretical error according to Eq. (1) is 0.48 mm, with a relative error of 1:3125. The ratio of measured error to theoretical error is 1.3. These values are consistent with those of James and Robson (2012) and Eltner et al. (2016) who stated that results in SfM-based 3D reconstructions do not usually reach theoretical errors that could be obtained with close range photogrammetry with convergent images. Other studies aimed at obtaining high precision SfM models at close range show higher error values because of either their image configuration network, usually in parallel strips with vertical imagery (Nouwakpo et al., 2014; Snapir et al., 2014), or their GCP configuration (Hänsel et al., 2016).

3.2. Digital elevation models

The height interpolation error was estimated using split-sample validation, which gave an average value of 0.106 mm. Given the homogeneity of the error values, a total DEM error with a value of

0.7 mm, obtained with Eq. (2), was assigned to all six DEMs. Fig. 4 shows the six raster DEMs



obtained in the study, represented with shading to better appreciate the relief.

Fig. 4. DEMs obtained in the experiment to quantify soil erosion produced by the five rain episodes.

3.3. Volumetric change from DoDs

The DEMs shown in Fig. 4 represent the topographic soil surface at certain time points, right after several corresponding rain episodes. The elevation difference between two successive surfaces, assuming they are in the same reference system, allows the calculation of the volume change. Comparisons between DEMs were made following the temporal sequence of the simulated rain episodes. Thus, a series of five DoDs corresponding to five successive episodes, hereinafter referred to as DoD_{0-1} , DoD_{1-2} , DoD_{2-3} , DoD_{3-4} , DoD_{4-5} , plus one corresponding to the entire period, DoD_{0-5} , were obtained (without applying any threshold). DODs were performed with the GIS tool

designed in ArcMap. Results are summarized in Table 2, whereas raster maps corresponding to the DoDs are shown in Figs. 5 and 8.

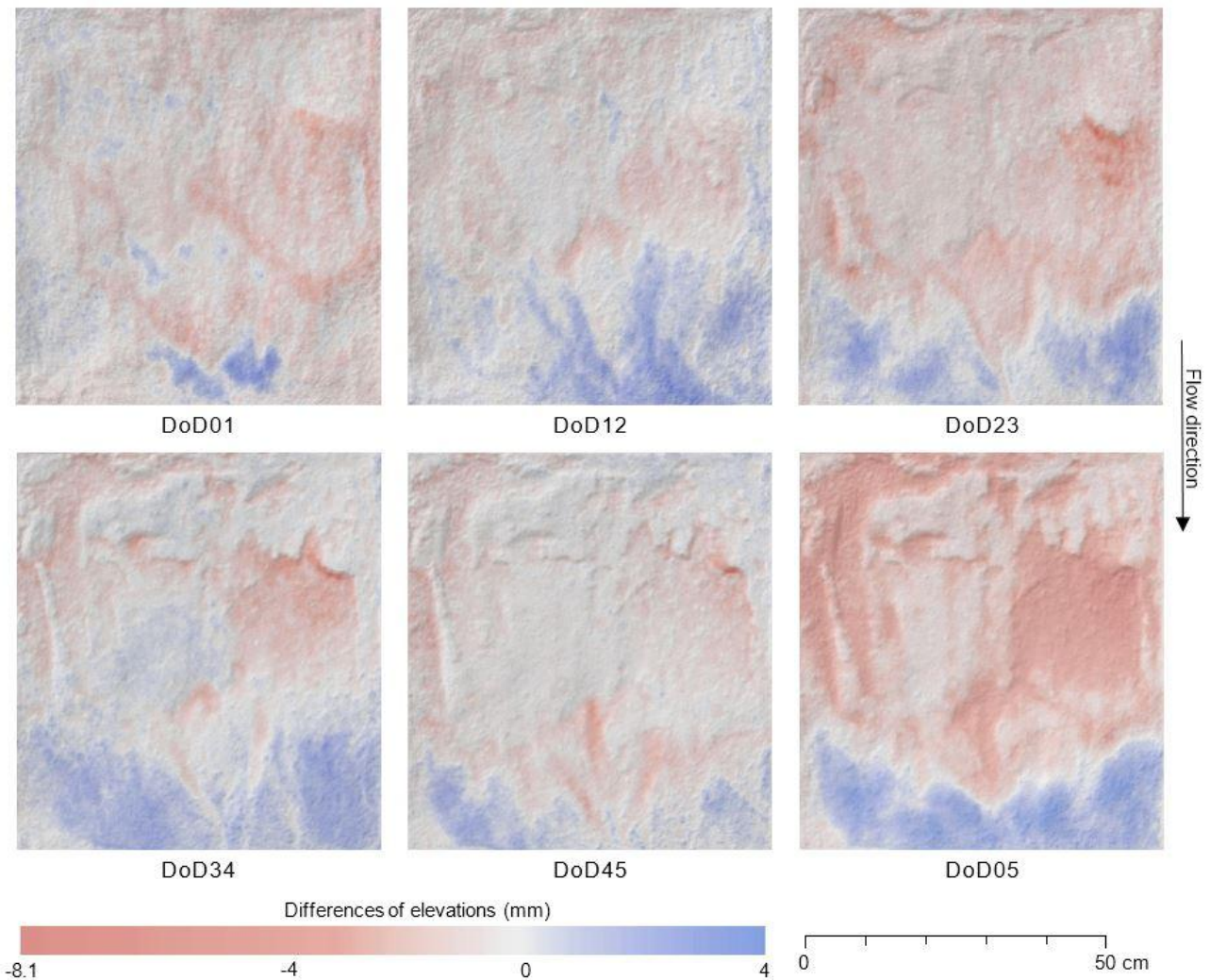


Fig. 5. DoDs. Differences of elevations for each rainfall episode (DoD01 to DoD45) and for all episodes (DoD05)-

Table 2 DoD results: Categorization (erosion, deposition and unchanged), net volume and cumulative volume.

Uncertainties calculated according to Lane et al. (2003).

	DoD	Erosion			Deposition			Unchanged		Net Volume (cm ³)	Cumulative Volume (cm ³)
		No. cells	% total	Volume (cm ³)	No. cells	% total	Volume (cm ³)	No. cells	% total		
No threshold	DoD ₀₋₁	387489	82.4	237.82 ± 0.62	80748	17.2	25.58 ± 0.28	2175	0.5	212.25 ± 0.68	212.25
	DoD ₁₋₂	290295	61.7	124.60 ± 0.53	177400	37.7	83.20 ± 0.42	2717	0.6	41.41 ± 0.68	253.65
	DoD ₂₋₃	380843	81.0	331.27 ± 0.61	88919	18.9	50.92 ± 0.30	650	0.1	280.34 ± 0.68	534.00
	DoD ₃₋₄	243101	51.7	149.73 ± 0.49	224305	47.7	101.72 ± 0.47	3006	0.6	48.01 ± 0.68	582.01
	DoD ₄₋₅	364037	77.4	172.21 ± 0.60	103210	21.9	30.58 ± 0.32	3165	0.7	141.63 ± 0.68	723.64
	DoD ₀₋₅	379764	80.7	889.22 ± 0.61	90524	19.2	165.58 ± 0.30	124	0.03	723.64 ± 0.68	
Threshold d 1 mm	DoD ₀₋₁	67561	14.4	86.50 ± 0.26	6141	1.3	8.89 ± 0.08	396710	84.3	77.61 ± 0.27	77.61
	DoD ₁₋₂	22059	4.7	29.02 ± 0.15	14579	3.1	16.83 ± 0.12	433774	92.2	12.18 ± 0.19	89.80
	DoD ₂₋₃	128616	27.3	173.66 ± 0.36	14180	3.0	19.17 ± 0.12	327616	69.6	154.49 ± 0.37	244.29

DoD ₃₋₄	54178	11.5	74.50 ± 0.23	26946	5.7	32.21 ± 0.16	389288	82.8	42.29 ± 0.28	286.57
DoD ₄₋₅	39809	8.5	51.68 ± 0.20	4163	0.9	4.80 ± 0.06	426440	90.7	46.88 ± 0.21	333.45
			415.40			81.90			333.45	

Table 2 shows that the total volume of erosion and deposition obtained by adding values corresponding to successive DoD is greater than that obtained in DoD₀₋₅. The estimated values of erosion/deposition from differences between topographical surfaces observed at different times can be negatively biased owing to compensating volumes of erosion and deposition between observations. Compensation occurs when there is a change between erosion and deposition at a point between two observations. The estimate of volume change is always less than the value that would be obtained if continuous monitoring of the topographical change were possible. Indeed it has been previously reported that compensation bias is greater when volumes of erosion and deposition are very similar (Lindsay and Ashmore, 2002). We examined this relationship between frequency and temporal differences in volume changes obtained from DEM as follows. The DoD obtained initially corresponds to the maximum temporal frequency for this experiment. To analyse the variation of the volume calculated by varying the frequency, new DEM differences with different time intervals of longer duration were obtained. The five series were:

- DoD₀₋₅
- DoD₀₋₃, DoD₃₋₅
- DoD₀₋₂, DoD₂₋₃, DoD₃₋₅
- DoD₀₋₂, DoD₂₋₃, DoD₃₋₄, DoD₄₋₅
- DoD₀₋₁, DoD₁₋₂, DoD₂₋₃, DoD₃₋₄, DoD₄₋₅

Fig. 6 shows the accumulated volume of erosion and deposition corresponding to each time sequence. It is clearly shown that the estimated volume decreases as the number of surfaces compared over the time period considered is reduced. Despite this negative relationship between temporal observation frequency and cumulative volume, net volume change (erosion less deposition) is independent of the sampling interval and remains constant for all intervals, with a value of 723.6 cm³.

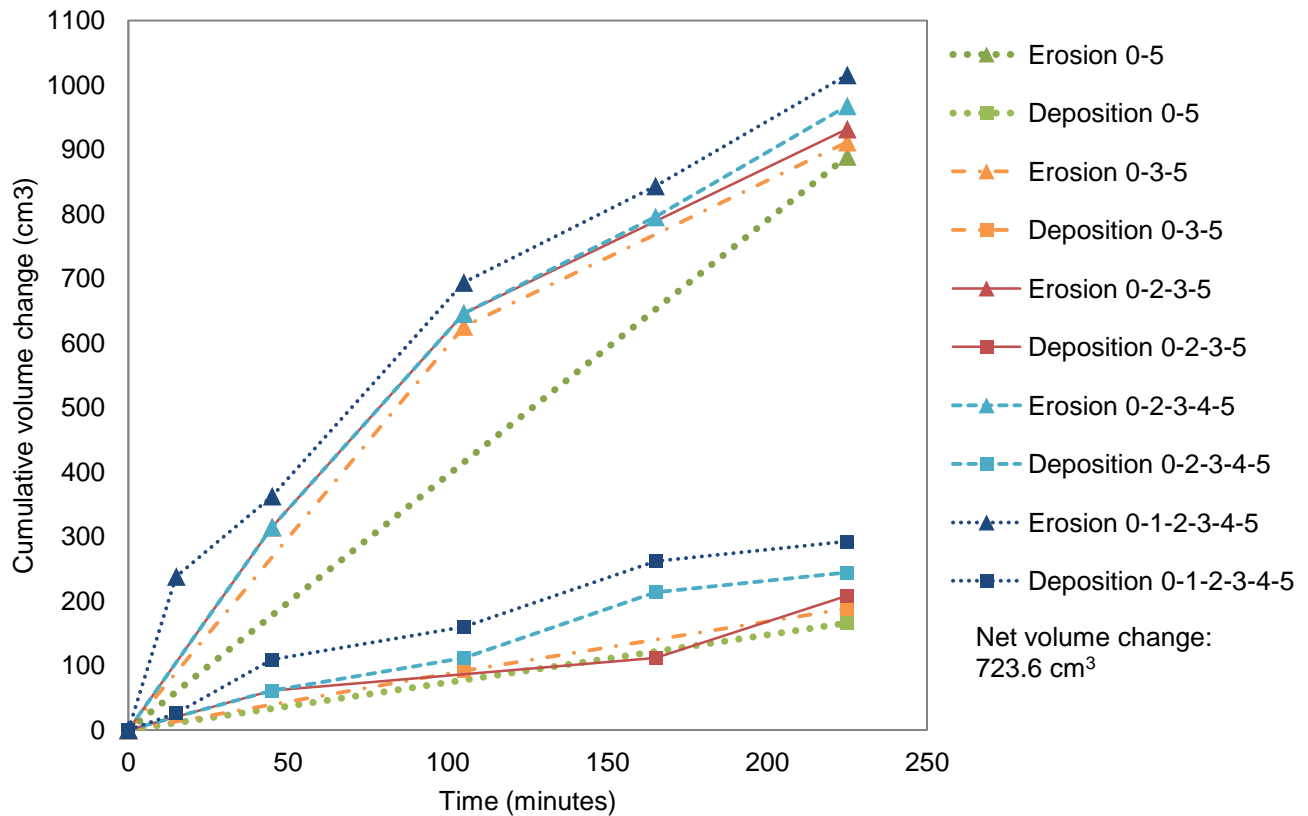


Fig. 6. Cumulative volume of erosion and deposition for different temporal frequencies.

This behaviour agrees with results observed by Lindsay and Ashmore (2002) in a laboratory experiment on an artificial channel of dimensions 3 x 11.5 m in medium-coarse sand. These authors applied a constant water discharge over a period of 100 min, obtaining 10 DEMs by photogrammetric techniques, with a temporal frequency of 10 min. Four series of DoD were obtained with intervals between surface comparisons of 10, 20, 50 and 100 min. In the experiment, they modelled the temporal relationship between frequency and volume through an inverse proportionality function and carried out a study of erosion-deposition compensation mechanisms observed on the channel. In our case, rills did not form because of the characteristics of the applied rainfall (namely low intensity and short duration). Therefore, areas of erosion and deposition produced were mostly diffuse, and changes between erosion and deposition between successive observations were frequently in the same area. Thus, it was not possible to determine the compensation mechanisms. However, our results are consistent with results reported by other authors (Lane et al., 1994; Lindsay and Ashmore, 2002).

The DoDs were initially calculated without applying any threshold. However, as discussed in Section 2.4, it is necessary to consider the uncertainty associated with each DEM involved in the

DoD. This is especially true in this study, where height differences can be quite small. Consequently, the final DoDs were obtained by establishing a minimum threshold to distinguish true elevation differences from noise. The threshold was calculated using Eqs. (3) and (4) from the DEM error values obtained previously:

$$LOD_{min} = E_{DoD_{1-2}} = \sqrt{(E_{MDE_1}^2 + E_{MDE_2}^2)} = \sqrt{2} \cdot E_{MDE} = \sqrt{2} \cdot 0.7 \cong 1 \text{ mm} \quad (5)$$

The same analysis of calculated volume changes depending on the temporal sampling frequency was also conducted on the thresholded DoDs (Fig. 7). We can see that the trend is reversed in this case, that is, the calculated volume increases with decreasing temporal frequency. Furthermore, the net volume is no longer constant, but varies in the same way. Similar behaviours were described in Schneider et al. (2011) and Brasington and Smart (2003), at different working scale. In our study, we decided to consider the original time sequence for volume and sediment calculations, which is consistent with the values of runoff collected in the experiment. The DoDs corresponding to all six successive episodes are DoD₀₋₁, DoD₁₋₂, DoD₂₋₃, DoD₃₋₄, and DoD₄₋₅.

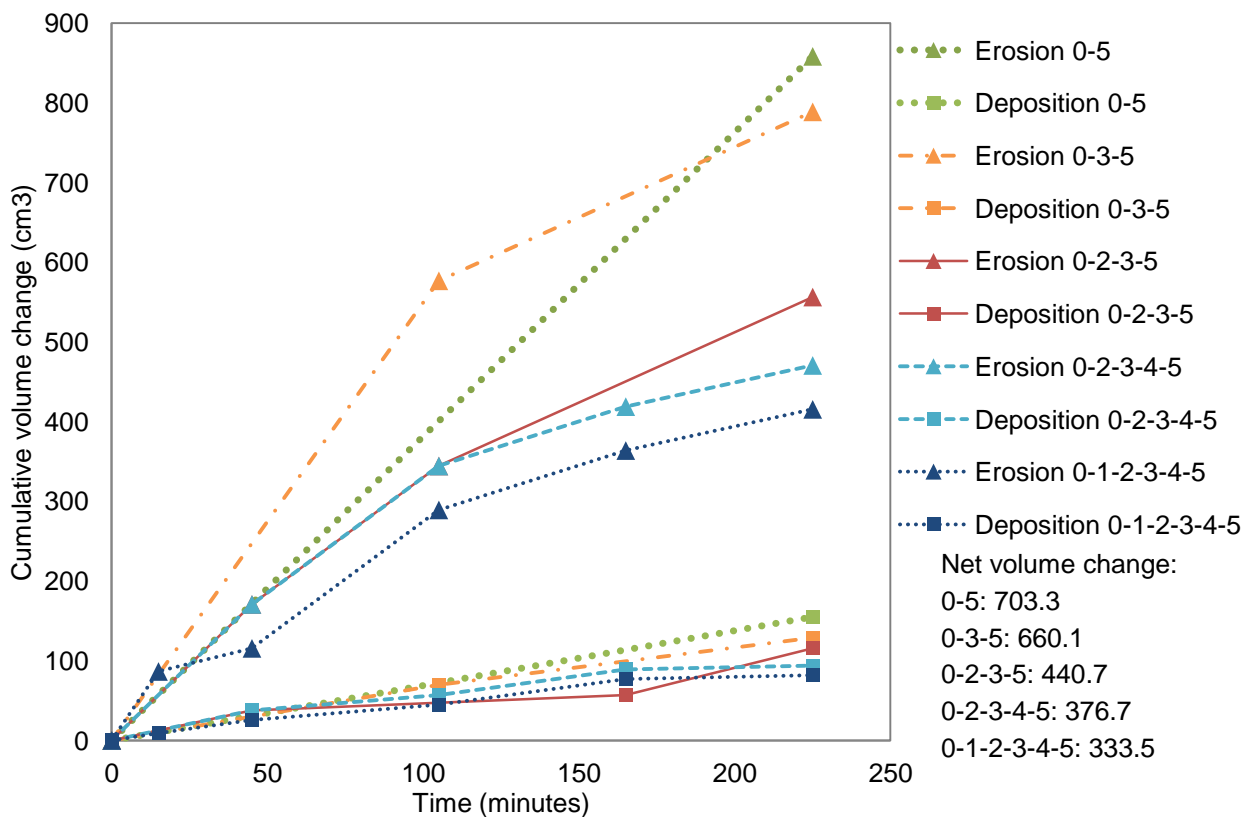


Fig. 7. Cumulative volume of erosion and deposition for different temporal frequencies with thresholded DoDs.

Table 2 shows the values of the DoDs after applying a threshold of 1 mm. Differences in elevations of the DoDs are mostly in the range of ± 3 mm, therefore the threshold value applied is essential to

obtain reliable results. Clearly, applying a threshold of 1 mm within this order of magnitude will produce very different results when compared to those from the direct difference between DEMs without considering any threshold. Table 2 shows, for example, that without thresholding, 82.4% of cells in DoD_{0-1} are classified within the erosion class, compared to 14.4% obtained when applying a significant change threshold of 1 mm. Fig. 8 shows classification into areas of erosion, deposition and unchanged classes for raw and thresholded DoDs.

ACCEPTED MANUSCRIPT

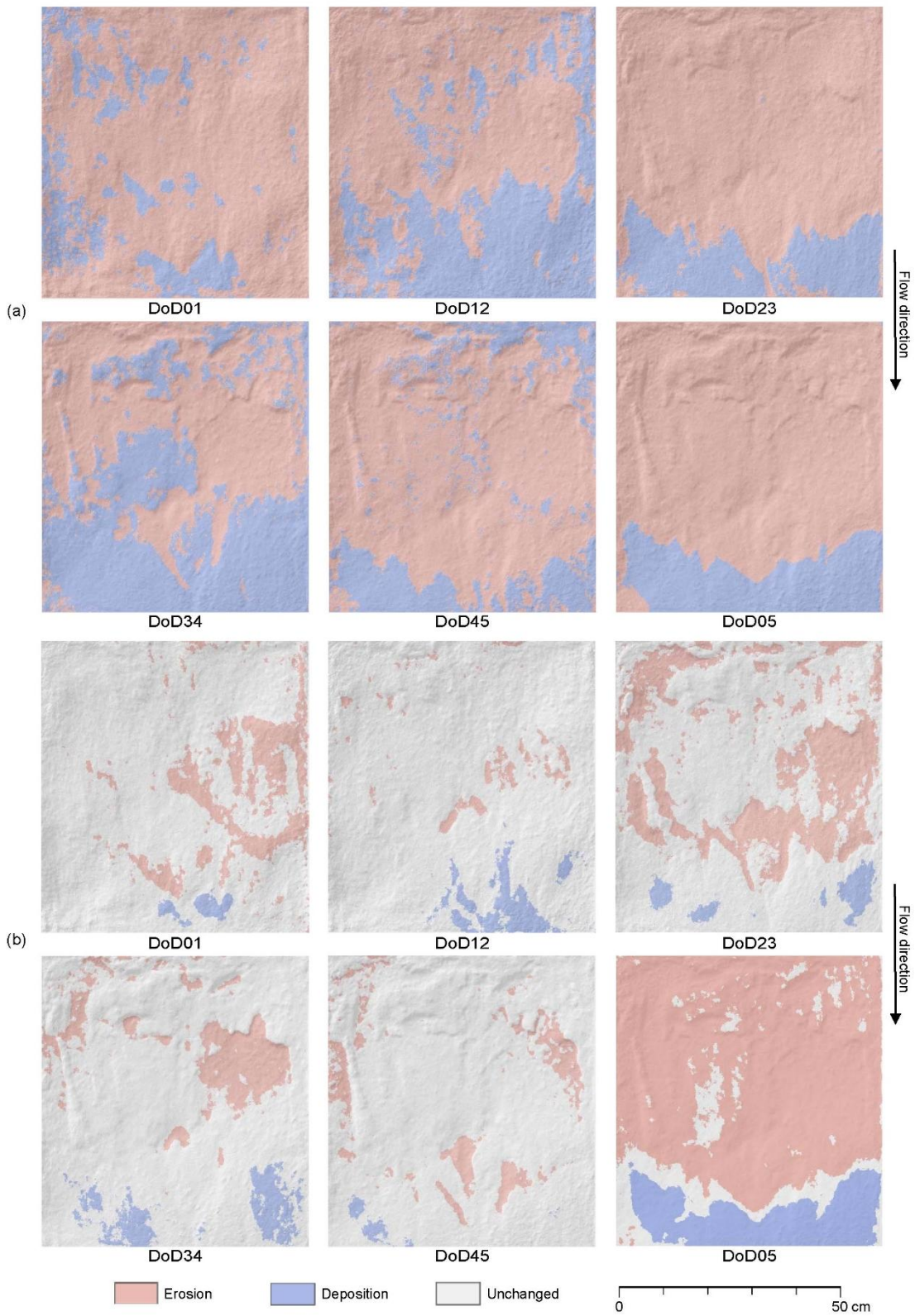


Fig. 8. DoDs classified into classes representing erosion, deposition and unchanged: (a) Without threshold; (b) with 1 mm threshold.

Fig. 9 shows the values of net volume change, calculated as the difference between erosion and deposition volumes. It should be noted that discrimination between non-significant changes (corresponding to variations in elevation less than 1 mm in absolute value) and significant changes is lower in DoDs with a smaller volume change, where there is a greater number of elevation differences of small magnitude.

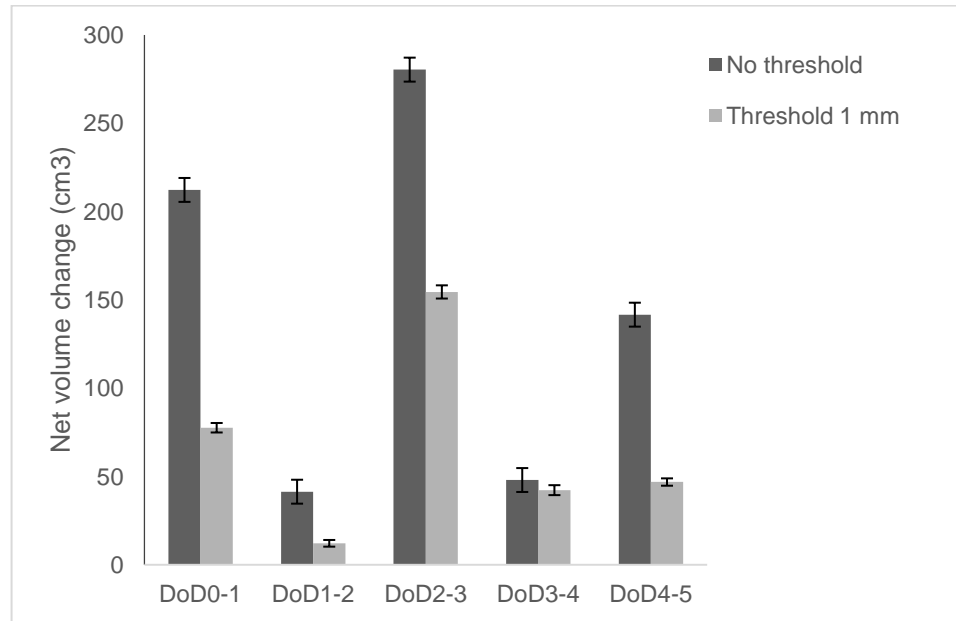


Fig. 9. Comparison of calculated net volume of the DoD without thresholding and with a threshold of 1 mm.

Error bars exaggeration factor = 10.

In order to analyse the evolution of volume changes over successive rainfall episodes, we plotted the cumulative net volume DoD (Fig. 10), which clearly shows the trend of increasing changes depending on the rainfall duration. Note also the obvious and remarkable difference between the estimates from the DoDs with and without threshold.

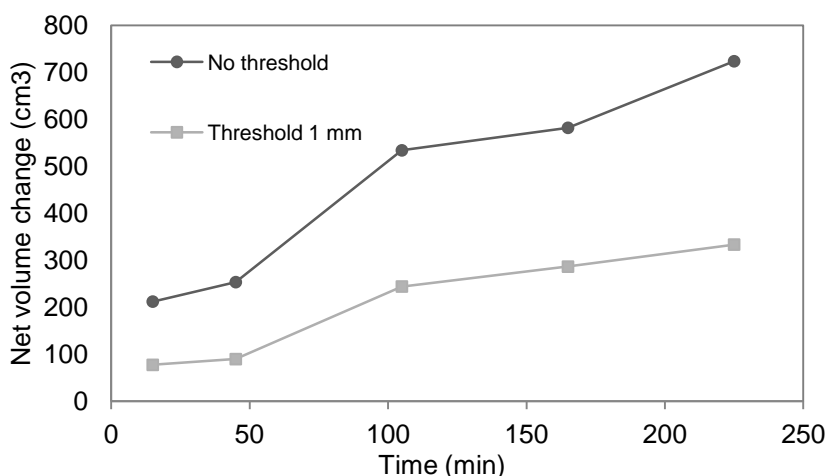


Figure 10 Cumulative net volume of DoD

3.4. Soil loss

In the experiment described in this paper, the sediment yield carried by the flow of water was collected and weighed. This allowed us to compare the measured sediment yield with estimates obtained from the DoD procedure. The net volume change obtained in the DoDs can be easily converted to soil loss weight using the bulk density value of the soil contained in the soil box. Table 3 contains the weight of the sediment yield calculated from the volume of net change (both for the DoD without threshold and with a 1 mm threshold), together with the weight of the measured sediment yield (Fig. 11). Infiltration was collected globally, without distinction between successive rain episodes, and is in the table for the sake of completeness.

Table 3 DoD results: mass (in g) of sediment calculated and sediment collected in the runoff and infiltration.

	Calculated sediment (g)				Collected sediment (g)		
	No threshold		Threshold 1 mm		Mass	Accumulated	
	Mass=Volume· ρ_b	Accumulated	Mass=Volume· ρ_b	Accumulated		Mass	Accumulated
DoD ₀₋₁	303.5 ± 8.5	303.5	111.0 ± 3.1	111.0	16.6	16.6	
DoD ₁₋₂	59.2 ± 1.9	362.7	17.4 ± 0.6	128.4	11.7	28.3	
DoD ₂₋₃	400.9 ± 11.3	763.6	220.9 ± 6.2	349.4	84.3	112.6	
DoD ₃₋₄	68.7 ± 2.2	832.3	60.5 ± 1.7	409.9	147.4	260.0	
DoD ₄₋₅	202.5 ± 5.7	1034.8	67.0 ± 1.9	476.9	128.4	388.4	
					Infiltration:	26.0	
	Bulk density: $\rho_b = 1.43 \pm 0.04 \text{ g/cm}^3$				Total:	414.4	

Fig. 11. Sediment (g) obtained from DoDs and collected in runoff. Error bars show uncertainties values from

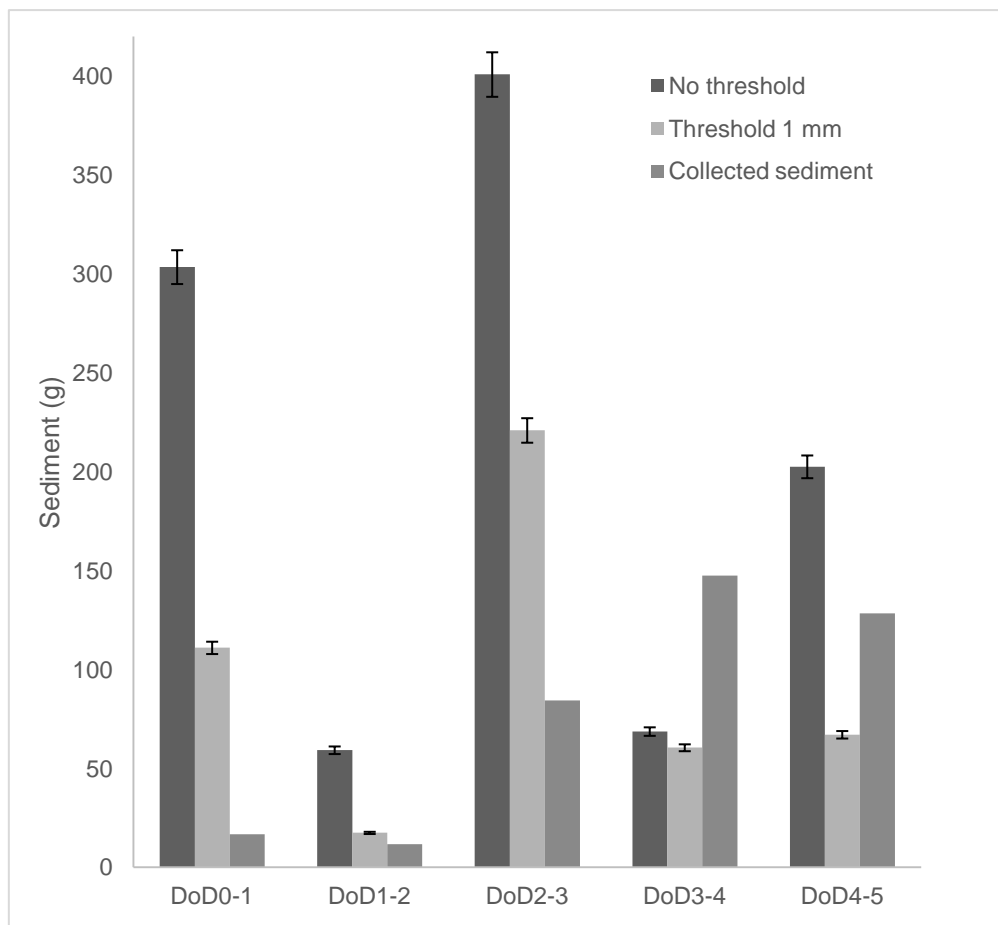


Table 3.

Fig. 12 shows the accumulated sediment yield (calculated and collected) in all five rainfall events. A very clear agreement between collected sediment yield and sediment determined from the thresholded DoDs is observed. The calculated values are systematically higher than their corresponding collected values, with an overestimation in accumulated sediment weight of 18%. It should be noted here that this value of total sediment collected does not include the sediment collected in the infiltration measurements. If infiltration is added to sediment yield by runoff, this difference decreases to 13%.

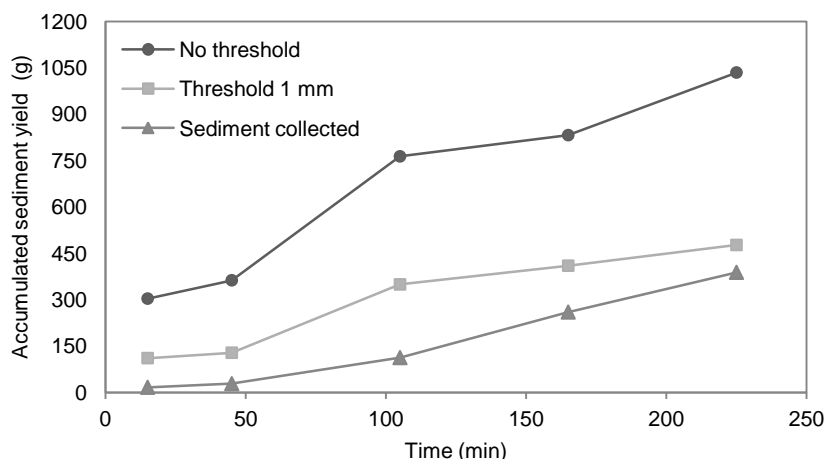


Fig. 12. Sediment accumulated, as calculated from the DoD and collected in runoff.

In analyzing the results, we must take into account that some of the factors that can affect our interpretations, such as soil composition, compaction or infiltration, were not considered in this study. It is also necessary to note that the conversion of volume changes to sediment weight depended on the value of the soil bulk density. Not only would a different value for soil bulk density produce a proportional change in the sediment weight, bulk density is a parameter that may vary spatially and can also undergo changes during the rain events. In this study, we assumed that bulk density was homogeneous across the box and during the duration of the experiment. However, changes in physical soil characteristics (such as pore space distribution) during successive rainfall events may be possible, especially in laboratory experiments with bare soil samples (Moritani et al., 2011). We addressed this issue by carefully preparing the soil box, which was wetted regularly to reach a stable density prior to conducting the experiment. In any case, the determination of the bulk density value is essential for the correct interpretation of the results and their conversion from DoD based volumes to sediment yield weight.

The data for the thresholded DoDs in Table 3 show in DoD₂₋₃ a calculated sediment value much higher (220.9 g) than the previous (17.4 g) and posterior (60.5 g) measurements. This value does not follow the trend observed in the sediment yield (Figs. 9 and 12). The sediment yield in Fig. 12 indicates that between the second and third rainfall episodes, the volume estimate, and therefore the derived sediment weight, is much greater than the actual collected sediment yield. However, calculated values for the remaining episodes seem to follow the same trend when compared to actual measured values from runoff. One possible interpretation is that there was some soil settling

during the third rainfall episode, between 45 and 105 min, which coincided with the start and stabilization of infiltration. A sudden settling or soil compaction would generate an increase in the volume change observed by the DoD approach that would not correspond to the amount of actual sediment yield collected over the same period. In this case, the DoD sediment weight would be greater than the actual sediment yield. Rieke-Zapp and Nearing (2005) conducted a laboratory rain simulation experiment on a soil tray and reported similar results, with calculated volumes greater than collected sediment yields (29% difference), which they attributed to soil settling issues. Heng et al. (2010) conducted a study with simulated rain of different intensities on plots with different slopes, and related changes in the morphology of the soil surface with bulk density changes caused by soil compaction and rainfall effects. Another factor that may influence the degree of soil settling is soil composition. Moritani et al. (2011) concluded that soil bulk density influences the accuracy of DEM-based erosion estimates. In soils with high bulk density, results of both estimated and collected sediment yields are more similar than in soils with lower density. In order to address this issue, soil bulk density was re-measured after the rainfall experiment. Two new soil samples were taken within the box, and the bulk density values were calculated using the standard procedure. The result was 1.45 g/cm^3 , which shows a slight increase of just 1.4% (0.02 g/cm^3) with respect to the initial value, along the same lines of Hänsel et al. (2016). While these values might be compatible with a slight soil settling, the small difference between the two bulk density values is lower than the standard error of the core sampling method itself (Raper and Erbach, 1987) which makes it impossible to confirm soil settling.

This study focuses on change detection and quantification from very small magnitude elevation differences, up to $\pm 3 \text{ mm}$. The experiment was designed to produce sheet erosion with low intensity rainfall, and no rills were formed in the experimental plot. In this regard, it is worth noting that most experiments at the microscale use higher intensity rainfall, e.g., 60 mm/h in Moritani et al. (2011), producing changes of higher magnitude that are easier to detect and estimate (Rieke-Zapp and Nearing, 2005; Heng et al., 2010). Our contribution in this paper is twofold. First, we assess the ability of the geomorphic change estimation approach to distinguish smaller changes between very similar surfaces of low roughness. Second, we suggest a validation of soil loss estimations with actual, total sediment yield collected during the experiment, not an estimated value from

sediment concentration sampling that can be a significant source of uncertainty (Hänsel et al., 2016). The error thresholding approach used, LOD_{min} , is the simplest but it has proven to provide good agreement with actual soil loss. An optimal image network configuration for the SfM-MVS photogrammetry and the correct georeferencing of DEMs were key elements in achieving these results. The procedure presented herein can be a suitable tool in studies of dynamic processes of small magnitude.

4. Conclusions

In this paper, we present a laboratory procedure to conduct rainfall-driven soil erosion experiments that provide insight into the errors involved in making very accurate measurements of small soil surface changes using DoDs based on photogrammetric SfM. The high average density of point clouds obtained by SfM-MVS photogrammetry allowed us to generate interpolated DEMs with millimetre resolution. The DoD technique was used to estimate volume changes experienced by the soil surface following successive rainfall events. The minimum level of detection defined by the quadratic composition of errors in individual DEMs proved to be a suitable parameter to define a threshold value to distinguish actual changes from errors. The choice of different threshold values in the DoDs led to volume differences as large as 60% when compared to the direct volumetric difference. We observed a reasonably good correlation between actual volumetric measurements of sediment yield and estimated values, but the computed sediment yields were systematically overestimated by 13%. Discrepancies may be influenced by undetected soil settling or other edaphic factors that increase volume differences without the loss of sediment. This study demonstrates the suitability of SfM-MVS photogrammetry to measure microscale soil surface changes, and illustrates the importance of minimum thresholding on DoDs.

References

- Afana, A., Solé-Benet, A., Pérez, J.C., 2010. Determination of soil erosion using laser scanners, in: Proceedings of the 19th World Congress of Soil Science, Soil Solutions for a Changing World. Brisbane, Australia, pp. 39–42.
- Armstrong, A., Quinton, J.N., Heng, B.C.P., Chandler, J.H., 2011. Variability of interrill erosion at low slopes. *Earth Surf. Process. Landforms* 36, 97–106. doi:10.1002/esp.2024

- Barazzetti, L., Scaioni, M., Remondino, F., 2010. Orientation and 3D modelling from markerless terrestrial images: Combining accuracy with automation. *Photogramm. Rec.* 25, 356–381. doi:10.1111/j.1477-9730.2010.00599.x
- Bertuzzi, P., Caussignac, J., Stengel, P., Morel, G., Lorendeau, J., Pelloux, G., 1990. An automated, noncontact laser profile meter for measuring soil roughness in situ. *Soil Sci.* 149, 169–178.
- Boix-Fayos, C., Martínez-Mena, M., Arnau-Rosalén, E., Calvo-Cases, A., Castillo, V., Albaladejo, J., 2006. Measuring soil erosion by field plots: Understanding the sources of variation. *Earth-Science Rev.* 78, 267–285. doi:10.1016/j.earscirev.2006.05.005
- Brasington, J., Langham, J., Rumsby, B., 2003. Methodological sensitivity of morphometric estimates of coarse fluvial sediment transport. *Geomorphology* 53, 299–316. doi:10.1016/S0169-555X(02)00320-3
- Brasington, J., Smart, R.M.A., 2003. Close range digital photogrammetric analysis of experimental drainage basin evolution. *Earth Surf. Process. Landforms* 28, 231–247. doi:10.1002/esp.480
- Bretar, F., Arab-Sedze, M., Champion, J., Pierrot-Deseilligny, M., Heggy, E., Jacquemoud, S., 2013. An advanced photogrammetric method to measure surface roughness: Application to volcanic terrains in the Piton de la Fournaise, Reunion Island. *Remote Sens. Environ.* 135, 1–11. doi:10.1016/j.rse.2013.03.026
- Butler, J.B., Lane, S.N., Chandler, J.H., 1998. Assessment of DEM quality for characterizing surface roughness using close range digital photogrammetry. *Photogramm. Rec.* 16, 271–291. doi:10.1111/0031-868X.00126
- Carrivick, J.L., Smith, M.W., Quincey, D.J., 2016. *Structure from Motion in the Geosciences*. Wiley-Blackwell, Chichester, UK. doi:10.1002/9781118895818
- Cerdà, A., 1999. Simuladores de lluvia y su aplicación a la Geomorfología: Estado de la cuestión. *Cuad. Investig. geográfica* 25, 45–84.
- Cerdà, A., Ibáñez, S., Calvo, A., 1997. Design and operation of a small and portable rainfall simulator for rugged terrain. *Soil Technol.* 11, 163–170. doi:10.1016/S0933-3630(96)00135-3

- Chan, K., 2006. Bulk density, in: Lal, R. (Ed.), *Encyclopedia of Soil Science*. CRC Press, Boca Raton, Florida, pp. 191–193.
- Chandler, J.H., 1999. Effective application of automated digital photogrammetry for geomorphological research. *Earth Surf. Process. Landforms* 24, 51–63. doi:10.1002/(SICI)1096-9837(199901)24:1<51::AID-ESP948>3.0.CO;2-H
- Darboux, F., Huang, C., 2003. An instantaneous-profile laser scanner to measure soil surface microtopography. *Soil Sci. Soc. Am. J.* 67, 92–99.
- Eltner, A., Kaiser, A., Castillo, C., Rock, G., Neugirg, F., Abellán, A., 2016. Image-based surface reconstruction in geomorphometry - merits, limits and developments. *Earth Surf. Dyn.* 4, 359–389. doi:10.5194/esurf-4-359-2016
- Erdogan, S., 2009. A comparison of interpolation methods for producing digital elevation models at the field scale. *Earth Surf. Process. Landforms* 34, 366–376. doi:10.1002/esp.1731
- Fonstad, M.A., Dietrich, J.T., Courville, B.C., Jensen, J.L., Carbonneau, P.E., 2013. Topographic structure from motion: a new development in photogrammetric measurement. *Earth Surf. Process. Landforms* 38, 421–430. doi:10.1002/esp.3366
- Fraser, C.S., 1996. Network design, in: Atkinson, K.B. (Ed.), *Close Range Photogrammetry and Machine Vision*. Whittle Publishing, Caithness, Scotland, pp. 256–281.
- Gessesse, G.D., Fuchs, H., Mansberger, R., Klik, A., Rieke-Zapp, D.H., 2010. Assessment of erosion, deposition and rill development on irregular soil surfaces using close range digital photogrammetry. *Photogramm. Rec.* 25, 299–318. doi:10.1111/j.1477-9730.2010.00588.x
- Gómez-Gutiérrez, Á., Schnabel, S., Berenguer-Sempere, F., Lavado-Contador, F., Rubio-Delgado, J., 2014. Using 3D photo-reconstruction methods to estimate gully headcut erosion. *Catena* 120, 91–101. doi:10.1016/j.catena.2014.04.004
- Hancock, G., Willgoose, G., 2001. The interaction between hydrology and geomorphology in a landscape simulator experiment. *Hydrol. Process.* 15, 115–133. doi:10.1002/hyp.143
- Hänsel, P., Schindewolf, M., Eltner, A., Kaiser, A., Schmidt, J., 2016. Feasibility of High-Resolution Soil Erosion Measurements by Means of Rainfall Simulations and SfM Photogrammetry.

Hydrology 3, 38. doi:10.3390/hydrology3040038

Haubrock, S.N., Kuhnert, M., Chabrillat, S., Güntner, A., Kaufmann, H., 2009. Spatiotemporal variations of soil surface roughness from in-situ laser scanning. *Catena* 79, 128–139. doi:10.1016/j.catena.2009.06.005

Heng, B.C.P., Chandler, J.H., Armstrong, A., 2010. Applying close range digital photogrammetry in soil erosion studies. *Photogramm. Rec.* 25, 240–265. doi:10.1111/j.1477-9730.2010.00584.x

Huang, C., Bradford, J.M., 1992. Applications of a laser scanner to quantify soil microtopography. *Soil Sci. Soc. Am. J.* 56, 14. doi:10.2136/sssaj1992.03615995005600010002x

James, L.A., Hodgson, M.E., Ghoshal, S., Latiolais, M.M., 2012. Geomorphic change detection using historic maps and DEM differencing: The temporal dimension of geospatial analysis. *Geomorphology* 137, 181–198. doi:10.1016/j.geomorph.2010.10.039

James, M.R., Robson, S., 2012. Straightforward reconstruction of 3D surfaces and topography with a camera: Accuracy and geoscience application. *J. Geophys. Res. Earth Surf.* 117, 1–17. doi:10.1029/2011JF002289

James, M.R., Robson, S., 2014. Mitigating systematic error in topographic models derived from UAV and ground-based image networks. *Earth Surf. Process. Landforms* 39, 1413–1420. doi:10.1002/esp.3609

Jester, W., Klik, A., 2005. Soil surface roughness measurement - Methods, applicability, and surface representation. *Catena* 64, 174–192. doi:10.1016/j.catena.2005.08.005

Kaiser, A., Neugirg, F., Rock, G., Müller, C., Haas, F., Ries, J., Schmidt, J., 2014. Small-scale surface reconstruction and volume calculation of soil erosion in complex moroccan Gully morphology using structure from motion. *Remote Sens.* 6, 7050–7080. doi:10.3390/rs6087050

Kasprak, A., Wheaton, J.M., Ashmore, P.E., Hensleigh, J.W., Peirce, S., 2015. The relationship between particle travel distance and channel morphology: Results from physical models of braided rivers. *J. Geophys. Res. Earth Surf.* 120, 55–74. doi:10.1002/2014JF003310

Kuipers, H., 1957. A relief meter for soil cultivation studies. *Neth. J. Agric. Sci.*

- Lane, S.N., Chandler, J.H., Richards, K.S., 1994. Developments in monitoring and modelling small-scale river bed topography. *Earth Surf. Process. Landforms* 19, 349–368.
- Lane, S.N., Westaway, R.M., Hicks, D.M., 2003. Estimation of erosion and deposition volumes in a large, gravel-bed, braided river using synoptic remote sensing. *Earth Surf. Process. Landforms* 28, 249–271. doi:10.1002/esp.483
- Lascelles, B., Favis-Mortlock, D., Parsons, T., Boardman, J., 2002. Automated digital photogrammetry: A valuable tool for small-scale geomorphological research for the non-photogrammetrist? *Trans. GIS* 6, 5–15. doi:10.1111/1467-9671.00091
- Li, Z., Chen, Z., 2012. Comparing two measuring methods of soil microtopography. 2012 1st Int. Conf. Agro-Geoinformatics, *Agro-Geoinformatics 2012* 408–411. doi:10.1109/Agro-Geoinformatics.2012.6311679
- Li, Z., Zhu, C., Gold, C., 2005. *Digital terrain modeling: principles and methodology*. CRC Press, Boca Raton.
- Lindsay, J.B., Ashmore, P.E., 2002. The effects of survey frequency on estimates of scour and fill in braided river model. *Earth Surf. Process. Landforms* 27, 27–43. doi:10.1002/esp.282
- Luhmann, T., Robson, S., Kyle, S., Boehm, J., 2013. *Close-Range Photogrammetry and 3D Imaging*, 2nd ed. Walter de Gruyter, Berlin/Boston. doi:10.1515/9783110302783
- Martínez-Casasnovas, J.A., 2003. A spatial information technology approach for the mapping and quantification of gully erosion. *Catena* 50, 293–308. doi:10.1016/S0341-8162(02)00134-0
- Marzoff, I., Poesen, J., 2009. The potential of 3D gully monitoring with GIS using high-resolution aerial photography and a digital photogrammetry system. *Geomorphology*. doi:10.1016/j.geomorph.2008.05.047
- Merrill, S.D., Huang, C., Zobeck, T.M., Tanaka, D.L., 2001. Use of the chain set for scale-sensitive and erosion-relevant measurement of soil surface roughness. D.E. Stott, R.H. Mohtar G.C. Steinhardt (eds). 2001. *Sustain. Glob. Farm. Sel. Pap. from 10th Int. Soil Conserv. Organ. Meet. held May 24-29, 1999 Purdue Univ. USDA-ARS Natl. Soil Eros. Resear* 585–591.
- Micheletti, N., Chandler, J.H., Lane, S.N., 2015. Structure from Motion (SfM) Photogrammetry, in:

Clarke, L.E., Nield, J.M. (Eds.), *Geomorphological Techniques*. British Society for Geomorphology, London.

Milan, D.J., Heritage, G.L., Large, A.R.G., Fuller, I.C., 2011. Filtering spatial error from DEMs: Implications for morphological change estimation. *Geomorphology* 125, 160–171. doi:10.1016/j.geomorph.2010.09.012

Moreno, R.G., Álvarez, M.C.C.D., Alonso, A.T., Barrington, S., Requejo, A.S., 2008. Tillage and soil type effects on soil surface roughness at semiarid climatic conditions. *Soil Tillage Res.* 98, 35–44. doi:10.1016/j.still.2007.10.006

Morgan, J.A., Brogan, D.J., Nelson, P.A., 2017. Application of Structure-from-Motion photogrammetry in laboratory flumes. *Geomorphology* 276, 125–143. doi:10.1016/j.geomorph.2016.10.021

Moritani, S., Yamamoto, T., Andry, H., Inoue, M., Nishimura, T., Fujimaki, H., Kimura, R., Saito, H., 2011. Monitoring of soil surface under wind and water erosion by photogrammetry, in: Lerner, J. (Ed.), *Wind Tunnels and Experimental Fluid Dynamics Research*. InTech, pp. 447–462.

Nouwakpo, S.K., James, M.R., Wertz, M.A., Huang, C.-H., Chagas, I., Lima, L., 2014. Evaluation of structure from motion for soil microtopography measurement. *Photogramm. Rec.* 29, 297–316. doi:10.1111/phor.12072

Podmore, T., Huggins, L., 1981. An automated profile meter for surface roughness measurements. *Trans. ASAE* 24, 663–666.

Raper, R., Erbach, D., 1987. Bulk density measurement variability with core samplers. *Trans. ASAE* 30, 878–881.

Reuter, H.I., Hengl, T., Gessler, P., Soille, P., 2009. Preparation of DEMs for geomorphometric analysis. *Dev. Soil Sci.* 33, 87–120. doi:10.1016/S0166-2481(08)00004-4.

Rieke-Zapp, D.H., Nearing, M.A., 2005. Digital close range photogrammetry for measurement of soil erosion. *Photogramm. Rec.* 20, 69–87. doi:10.1111/j.1477-9730.2005.00305.x

Rieke-Zapp, D.H., Wegmann, H., Santel, F., Nearing, M., 2001. Digital photogrammetry for measuring soil surface roughness. *Proc. Am. Soc. Photogramm. Remote Sens. 2001 Conf.*

Gatew. to New Millenn. 1–8.

- Saleh, A., 1993. Soil roughness measurement - chain method. *J. Soil Water Conserv. Soc.* 48, 527–529. doi:10.4016/28481.01
- Schneider, A., Gerke, H.H., Maurer, T., 2011. 3D initial sediment distribution and quantification of mass balances of an artificially-created hydrological catchment based on DEMs from aerial photographs using GOCAD. *Phys. Chem. Earth* 36, 87–100. doi:10.1016/j.pce.2010.03.023
- Smith, M.W., Vericat, D., 2015. From experimental plots to experimental landscapes: topography, erosion and deposition in sub-humid badlands from Structure-from-Motion photogrammetry. *Earth Surf. Process. Landforms* 40, 1656–1671. doi:10.1002/esp.3747
- Smith, M.W., Carrivick, J.L., Quincey, D.J., 2016. Structure from motion photogrammetry in physical geography. *Prog. Phys. Geogr.* 40, 247–275. doi:10.1177/0309133315615805
- Smith, S.L., Holland, D.A., Longley, P.A., 2005. Quantifying interpolation errors in urban airborne laser scanning models. *Geogr. Anal.* 37, 200–224. doi:10.1111/j.1538-4632.2005.00636.x
- Snapir, B., Hobbs, S., Waine, T.W., 2014. Roughness measurements over an agricultural soil surface with Structure from Motion. *ISPRS J. Photogramm. Remote Sens.* 96, 210–223. doi:10.1016/j.isprsjprs.2014.07.010
- Stroosnijder, L., 2005. Measurement of erosion: Is it possible? *Catena* 64, 162–173. doi:10.1016/j.catena.2005.08.004
- Vidal Vázquez, E. y P.G.A., 2003. Evolución del microrrelieve de la superficie del suelo medido a diferentes escalas. *Estud. la Zo. No Saturada del Suelo* 6, 203–208.
- Wackrow, R., Chandler, J., 2011. Minimising systematic error surfaces in digital elevation models using oblique convergent imagery. *Photogramm. Rec.* 26, 16–31.
- Wenzel, K., Rothermel, M., Fritsch, D., Haala, N., 2013. Image acquisition and model selection for Multi-View Stereo. *Int. Arch. Photogramm. Remote Sens. Spat. Inf. Sci.* XL, 251–258. doi:10.5194/isprsarchives-XL-5-W1-251-2013
- Westoby, M.J., Brasington, J., Glasser, N.F., Hambrey, M.J., Reynolds, J.M., 2012. “Structure-

from-Motion” photogrammetry: A low-cost, effective tool for geoscience applications. *Geomorphology* 179, 300–314. doi:10.1016/j.geomorph.2012.08.021

Wheaton, J.M., Brasington, J., Darby, S.E., Sear, D.A., 2010. Accounting for uncertainty in DEMs from repeat topographic surveys: improved sediment budgets. *Earth Surf. Process. Landforms* 35, 136–156. doi:10.1002/esp.1886

Williams, R.D., 2012. DEMs of Difference. *Geomorphol. Tech.* 2, 1–17.

Yang, M.-D., Chao, C.-F., Huang, K.-S., Lu, L.-Y., Chen, Y.-P., 2013. Image-based 3D scene reconstruction and exploration in augmented reality. *Autom. Constr.* 33, 48–60. doi:10.1016/j.autcon.2012.09.017